Terrain-Dependent Slip Risk Prediction for Planetary Exploration Rovers

Terrain-Dependent Slip Risk Prediction for Planetary Exploration Rovers

Masafumi Endo†*, Shogo Endo†, Kenji Nagaoka‡, and Kazuya Yoshida†

†*Department of Aerospace Engineering, Graduate School of Engineering, Tohoku University, Japan*
‡*Department of Mechanical and Control Engineering, Graduate School of Engineering, Kyushu Institute of Technology, Japan*

SUMMARY

Wheel slip prediction on rough terrain is crucial for secure, long-term operations of planetary exploration rovers. Although rough, unstructured terrain hampers mobility, prediction by modeling wheel-terrain interactions remains difficult owing to unclear terrain conditions and complexities of terramechanics models. This study proposes a vision-based approach with machine learning for predicting wheel slip risk by estimating the slope from 3D information and classifying terrain types from image information. It considers the slope estimation accuracy for risk prediction under sharp increases in wheel slip due to inclined ground. Experimental results obtained with a rover testbed on several terrain types validate this method.

KEYWORDS: Planetary exploration rovers; Machine learning; Wheel slip prediction; Exteroceptive sensing; Slope estimation.

1. Introduction

Planetary exploration rovers have been used for conducting detailed investigations of extraterrestrial surfaces such as those of Moon and Mars. During these missions, rovers have to be operated with weak communication signals and nonnegligible communication lag. To overcome these constraints, rovers have been required to automatically recognize their surrounding environment, detect obstacles, and travel through uncharted regions. For example, the *Spirit* and *Opportunity* rovers (National Aeronautics and Space Administration (NASA)) used conventional perception strategies that evaluated their surrounding environments by using stereo vision and detecting geometric obstacles.[1] Although this approach enabled successful long-term operation of the rovers, loose, granular materials on celestial surfaces can make the rovers wheels slip and, in the worst case, can cause the rover to get stuck without the possibility of recovery. In the Mars Science Laboratory (MSL) mission, *Curiosity* experienced excessive wheel slip in the Hidden Valley.[2] The terrain here comprised rippled sand that seemed safe and nonhazardous; nonetheless, *Curiosity* was forced to avoid these nongeometric obstacles.

To assess wheeled robots mobility on rough terrain, the mechanical phenomena occurring in wheel-terrain interaction have been studied in the field of terramechanics.[3] Slip causes a lack of movement when wheeled robots traverse terrain. Although considering wheel slip is crucial for rovers, the complexity of modeling the highly nonlinear characteristics of rover-terrain interaction makes it difficult to evaluate and predict rovers traversability to accomplish autonomous operations.

---

* Corresponding author. E-mail: masafumi.endo@ieee.org

Fig. 1. The Hidden Valley on Mars ©NASA/JPL. *Curiosity* experienced excessive wheel slip here and failed to traverse this region although it is relatively flat. At the beginning of the mission, *Curiosity* was commanded to travel on the flat surface and avoid obstacles such as rocks; however, wheel slip occurred owing to loose sand with megaripples. Wheel traces on these megaripples indicated that *Curiosity* gave up traversing this surface and turned back to avoid getting stuck.

Visual information provides rovers with more clues to predict wheel slip from a distance. Geometric information of the terrain topography, such as steep slopes that cause wheel slip,[4] can be obtained from 3D measurements through stereo vision. Further, visual characteristics such as color and texture provide semantic descriptions of terrain types to evaluate rovers mobility. Both of these clues are obtained from a distance; hence, exteroceptive sensing can potentially be used to predict wheel slip before entering the hazardous area by estimating slopes and assessing terrain types for rovers operating on rough terrain.

This study proposes a method to predict the wheel slip risk for a rover operating on rough terrain. This method involves two procedures: (1) slope estimation from 3D information and (2) terrain classification from images by using a machine-learning classifier. A regression curve optimized with previously experienced data is used as a slip versus slope relation to predict the wheel slip risk corresponding to the estimated slope angle and classified terrain. The terrain-dependent slip risk, classified as low, medium, or high, is predicted using the slip versus slope relation in consideration of the slope estimation accuracy. Thresholds are set for each terrain type because different terrain types have different impacts on the rover. Experimental results obtained using a rover testbed operated on several terrain types are presented to validate the proposed approach.

The rest of this paper is organized as follows. Section 2 defines wheel slip and discusses related work. Section 3 presents details of the proposed slip risk prediction approach. Section 4 describes the experiment for validating the proposed approach, including detailed information of the testbed, data collection, and experimental conditions. Section 5 presents experimental results validating the performance of the proposed slip risk prediction approach. Finally, Section 6 concludes this paper.

2. Related Work

2.1. Background on Slip

Wheel slip is considered one of the critical factors for rovers to traverse rough terrain. Wheel slip is quantitatively described by the slip ratio.[5] The slip ratio s is a proportion of the desired and actual traveling velocities and is expressed as follows:

$$s = \frac{r\omega - v}{r\omega} = 1 - \frac{v}{r\omega}(0 \leq s \leq 1),\tag{1}$$

where v is the actual traveling velocity, and r and ω are the radius and angular velocity of the wheel, respectively, as shown in Fig. 2. The slip ratio represents the degree of longitudinal slip. A positive slip ratio implies that a rover is traveling slower than commanded, and a slip ratio of 1 implies that the rover is completely stuck in rough terrain.

2.2. Traversability Assessment

Mobile robots must have vision so that they can assess their traversability. NASA's Mars Exploration Rover (MER) mission conducted geometric analyses using a stereo camera that detected natural obstacles, such as small rocks, to assess whether the rovers wheels could get over them.[1] However, this approach could not solve problems caused by rough terrain, such as wheel slip, sinkage, and complete immobilization of the rover, because geometric information does not contain semantic characterizations of the physical properties of the target terrain.

Learning-based terrain assessment approaches using visual information have been actively studied to enable mobile robots to detect such nongeometric hazards and avoid wheel slip on rough terrain. These approaches afford two main advantages: traversability can be predicted to detect potential risks before entering the region in front of the robots and modeling of complex wheel-terrain interactions can be avoided. Halatci et al.[6] presented a multisensor terrain classification method that applied Bayesian fusion of individual support vector machines (SVMs) using color, texture, and depth information acquired by stereo imagery. Brooks et al.[7] expanded this approach to self-supervised terrain classification by associating exteroceptive data with proprioceptive wheel vibration data. Otsu et al.[8] proposed co- and self-training approaches that classified the surrounding terrain of a rover with lesser image data. Several studies have also investigated traversability prediction as well as terrain classification. Berczi et al.[9] showed that Gaussian process (GP) classifiers enable learning and assessing the traversability of terrain with a high-dimensional representation. Schilling et al.[10] implemented a geometric and visual terrain classification method that predicts terrain traversability in a mixture of environments with less training data. Higa et al.[11] proposed a vision-based approach that remotely predicts the energy consumed by rovers when driving to search for and traverse desirable paths on rough terrain. Wheel slip is one of the indexes used to assess traversability. Angelova et al.[12] applied a mixture of expert models for combining the results of terrain classification and terrain-dependent slip prediction using locally weighted projection regression (LWPR) to predict wheel slip from visual information. Cunningham et al.[13] used GP regression for considering the uncertain wheel-terrain relation for each terrain, which was classified using convolutional neural networks (CNNs). Skonieczny et al.[14] evaluated the trafficability risk of planetary rovers using a slip-slope table specific to each terrain, which adapts to variable slip versus slope data, and by assigning thresholds between low, medium, and high slip risk. These thresholds were defined by considering the hazardous slip ratio to be 0.2; however, these fixed thresholds could cause incorrect wheel slip risk evaluation owing to the uncertainty of slope estimation. Although the slip risk monotonically increases with increasing slope, wheel slip trends differ with the terrain type being traversed. For instance, uneven gravel terrain causes a sudden increase in wheel slip, and the slip versus slope relation on
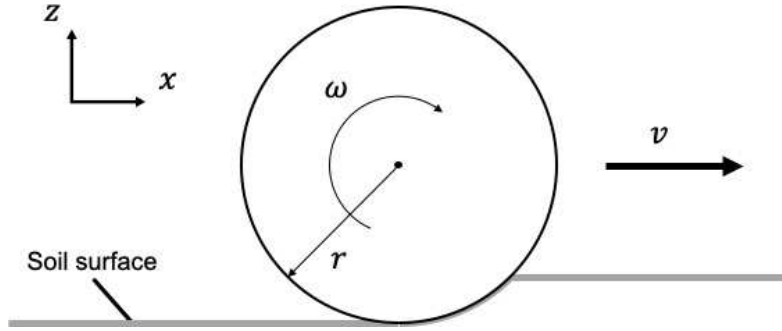
Fig. 2. Longitudinal wheel slip on loose soil.

terrain consisting of homogeneous loose sand is almost linear. Thus, terrain-dependent thresholds are a more reasonable criterion for evaluating the slip risk of wheeled robots on rough terrain.

This study predicts the slip risk of a rover traversing rough terrain. The main idea is to enable the rover to discover hazardous region from a distance. Two factors—terrain slope and terrain type—that affect the degree of wheel slip are investigated using visual information to predict wheel slip corresponding to the obtained slope angle and terrain classification. The proposed approach differs from the above-described methods in that it introduces terrain-dependent thresholds for the slip versus slope relation for the rover to predict the wheel slip risk. The mean absolute error (MAE) between the estimated slope angle and the ground truth value is used as a margin to bound the thresholds. By using this prediction method, (1) the characteristic wheel slip risk is predicted on the target region of the terrain and (2) the MAE enables avoiding underestimating the slip risk owing to the uncertain terrain surface.

3. Overview of Slip Risk Prediction

This section presents an overview of the proposed approach for learning the relation between visual information and wheel slip based on data obtained from both exteroceptive and proprioceptive sensors. Wheel slip results from wheel-terrain interactions, and the amount of wheel slip depends on geometric conditions such as the slope, state, and composition of the terrain. Therefore, the proposed slip risk prediction approach is based on slope estimation and terrain classification, as shown in Fig. 3, and the use of visual information from an RGB-D sensor. The slip risk is finally predicted by assessing the classified terrain and slip ratio corresponding to the estimated slope angle.

3.1. Slope Estimation

The slope estimation procedure acquires the slope angle of terrain in front of the rover by calculating the least squares plane using 3D point clouds acquired from an RGB-D sensor. To remove outliers in the point cloud data, the RANdomized SAmple Consensus (RANSAC) algorithm is applied as follows:[16]

1. Select n sample points at random from 3D point clouds $\mathcal{U}$.
2. Calculate the plane equation that minimizes the sum of squares of plane $\mathcal{Z}$ and n points.
3. Evaluate the coincidence between $\mathcal{U}$ and $\mathcal{Z}$ calculated in step 2.
4. Repeat from step 1 to obtain the least squares plane $\mathcal{Z}'$.
5. Calculate slope angle θ as the pitch angle for the rover coordinate $\sum_{\text{Rover}}\{X, Y, Z\}$ by using the following equation:

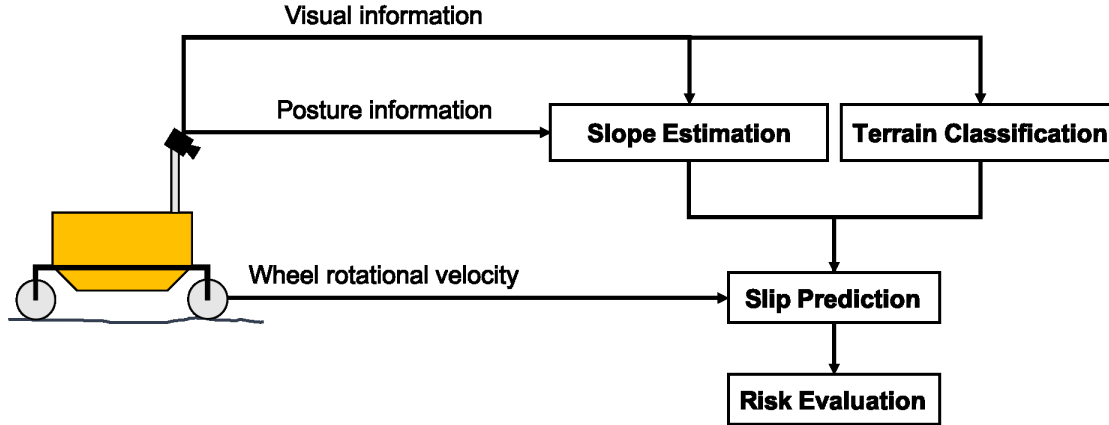$$\theta = -\tan^{-1}\frac{\partial \mathcal{Y}}{\partial \mathcal{Z}'}. \tag{2}$$

Fig. 3. Architecture of proposed slip prediction approach. Input posture and 3D information acquired using the IMU and RGB-D sensor, respectively, are used for slope estimation, and image data is used for terrain classification. Wheel slip is predicted by integrating both the slope estimation and the terrain classification results.
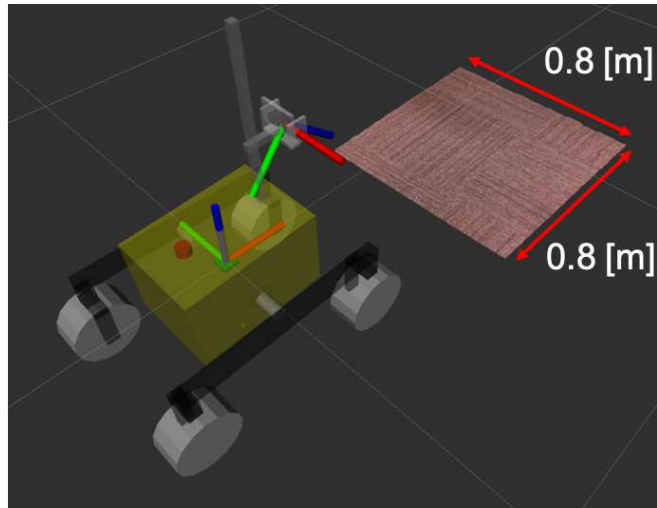

Fig. 4. ROI in front of rover in RViz 3D visualization tool. The ROI is expressed by a 3D point cloud of 0.8 m^2. Two coordinate systems are used for the camera and the rover body, respectively, and 3D point cloud information is converted from the camera into the body coordinate system for slope estimation.

This procedure also reflects the rover posture by acquiring data from inertial measurement units (IMUs) and potentiometers in the rovers suspension mechanism, as discussed in Section 4. The region of interest (ROI) for slope estimation is 0.8 m^2 in front of the rover, as shown in Fig. 4, considering the effective measurement range of the RGB-D sensor.

3.2. Terrain Classification

To assess the distinctive terrain type of a given region, terrain is classified by a machine-learning classifier using images as the input. Terrain classification mainly consists of two procedures: feature extraction and classifier training.

Before feature extraction, the image viewpoint is converted from the camera view into a top view for evaluating the region corresponding to the ROI for slope estimation. Inverse perspective transformation is applied for image transformation preprocessing.[17]

Visual features are then selected and extracted from the converted RGB image acquired using the exteroceptive sensor. In this study, color- and texture-based features are applied for classification. To obtain color-based features, the original RGB image
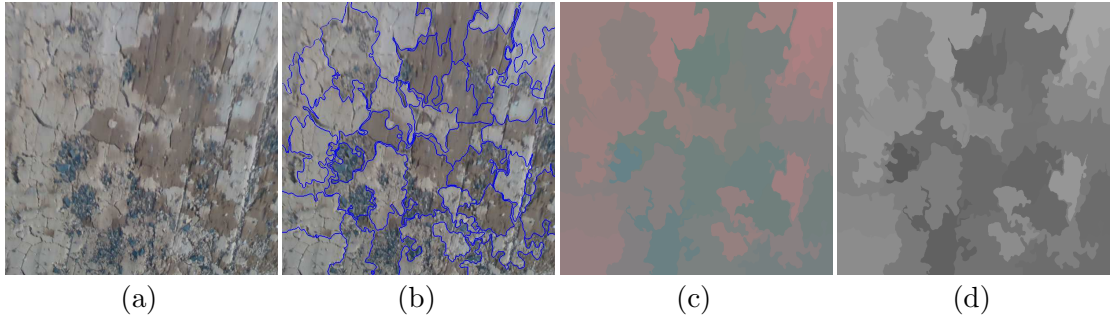
Fig. 5. (a) Original visual image of cracked-ground region. (b) Segmented image by superpixels. Blue lines are boundaries for visually homogeneous pixels. (c) Mean color of L*a*b* color space. (d) Mean color of gray-scale image used for texture extraction.

is converted to the L*a*b* color space, where L* represents lightness, and a* and b* represent color dimensions. The mean values of a* and b* inside a patch are calculated to compose a two-element feature vector, and the L* value is not used to reduce the effect of lighting conditions. Texture-based features are also extracted from the obtained images. A texture is a measure of the local spatial variation of image intensity. In this study, energy and contrast, which express the gray-scale distribution homogeneity and image sharpness, respectively, are calculated from the gray level co-occurrence matrix (GLCM). To decompose each image, a superpixel representation is applied instead of fixed-sized patches. Each superpixel agglomerates visually homogeneous pixels while respecting natural scene boundaries.[18] Specifically, simple linear iterative clustering (SLIC), in which a k-means clustering approach is used to efficiently generate superpixels, is used to decompose the image into image patches for feature extraction.[19] Fig. 5 shows a sample image of this feature extraction process.

Finally, a classifier is trained using the color- and texture-based features. In this study, the gradient boosting decision tree (GBDT) classifier is used for solving the classification problem. Gradient boosting is a type of ensemble learning that consists of multiple weak prediction models.[20] In particular, a GBDT comprises multiple decision trees that recursively partition the input space for prediction.[21] Thus, the output of GBDT, $p(c|\mathbf{v})$, is expressed by the posterior probability $p_t(c|\mathbf{v})$ of each decision tree as follows:

$$p(c|\mathbf{v}) = \frac{1}{T} \sum_{t=1}^{T} p_t(c|\mathbf{v}), \tag{3}$$

where c, $\mathbf{v}$, and T are the classes, input feature vectors, and number of decision trees, respectively. This learning method can achieve better predictive performance and avoid overfitting by reflecting the results of trained classifiers on new ones.

3.3. Terrain-Dependent Slip Risk Prediction

3.3.1. Definition of Slip Risk. As mentioned in Section 2.1., wheel slip is quantitatively described by the slip ratio. This study classifies the slip ratio as low $(0 < s \leq 0.3)$, medium $(0.3 < s \leq 0.6)$, and high $(0.6 < s)$. In previous literature[22],[23] the slip ratio was distinguished into three classes, as in the present study, by referring to the behaviors of a single-wheel testbed with a flight spare wheel for *Curiosity*. Another study noted that wheels exhibit a sharp increase in slip for slip ratio of 0.2–0.3.[24] Similarly, the experimental results of the present study, as presented later, indicate that the rover travels steadily for slip ratio of up to 0.3 but becomes unstable when the slip ratio reaches 0.6. Based on both previous literature and the rovers mobility in this study, this definition is used as a reasonable indicator for evaluating the wheel slip risk.

3.3.2. Slip Risk Prediction. Before risk prediction, the slip ratio is predicted from a regression curve using the acquired slip versus slope data as inputs. The predicted slip ratio s and a linear basis function $y(\mathbf{x}, \mathbf{w})$ are expressed as follows:

$$s = y(\mathbf{x}, \mathbf{w}) + \epsilon, \tag{4}$$

$$y(\mathbf{x}, \mathbf{w}) = \sum_{j=0}^{M-1} w_j \phi_j(\mathbf{x}) = \mathbf{w}^{\mathrm{T}} \boldsymbol{\phi}(\mathbf{x}.) \tag{5}$$

where ϵ, $\mathbf{x}$, and $\mathbf{w}$ are the error, input variables, and parameters, respectively, and $\boldsymbol{\phi}(\mathbf{x})$ are basis functions. To minimize ϵ, $\mathbf{w}$ is derived by the following equation:

$$\min E(\mathbf{w}) = \frac{1}{2} \sum_{n=1}^{N} \left\{ s - \mathbf{w}^{\mathrm{T}} \boldsymbol{\phi}(\mathbf{x}) \right\}^2. \tag{6}$$

In this study, the Gaussian basis function is used as the basis function:

$$\phi_j(x) = \exp\left\{ -\frac{(x - \mu_j)^2}{2t^2} \right\}, \tag{7}$$

where μ_j is the location of the basis function in the input space and t, its spatial scale.[25]

Then, the slip risk is predicted by comparing the acquired regression to the thresholds mentioned in Section 3.3.1. While the three classes are defined as slip risk common to the terrain, this study redefines the slip risk to a terrain-dependent one by reflecting the slope estimation accuracy. Fig. 6 shows the concept of deciding the terrain-dependent threshold for risk prediction. The threshold common to terrain, such as 0.3 and 0.6, is expressed as

$$s = f(\phi). \tag{8}$$

To redefine the terrain-dependent threshold in consideration of the slope estimation accuracy, MAE σ is subtracted from ϕ as follows:

$$s' = f(\phi - \sigma) = f(\phi'), \tag{9}$$

$$MAE : \sigma = \frac{1}{n} \sum_{i=1}^{n} |f_i - y_i|, \tag{10}$$

where f_i and y_i are the estimated slope angle value and ground truth value, respectively. Through the above procedure, the thresholds of each terrain for risk prediction are shifted from common points (ϕ, s) to terrain-dependent ones (ϕ', s'). Note that the regression curve for each terrain has a different inclination because different terrain properties result in specific wheel-terrain interactions. For instance, while wheel slip on homogeneous loose sand monotonously increases as the slope of the traversing surface increases, a rovers behavior on gravel terrain becomes more unpredictable owing to the uneven constitution
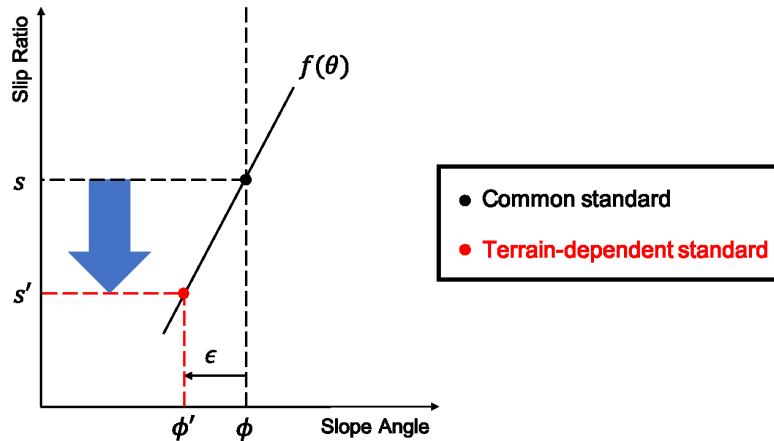
Fig. 6. Concept of deciding new threshold considering inclination of function.

of this terrain. The slip risk is redefined in consideration of the slope estimation accuracy for dealing with the terrain-dependent inclination of the regression curve, especially when a sharp increase in slip ratio results in a difference between the actual and predicted slip risk.

4. Experiment
An experiment was performed to validate the proposed approach using datasets including images, 3D point clouds, and slip versus slope data collected with a four-wheeled rover testbed operating on rough terrain. This section describes the testbed, data collection, and experimental conditions in detail.

4.1. Testbed
In this study, the El-Dorado IIB four-wheeled rover testbed (Fig. 7) is used for data collection. Table I lists the specifications of the testbed. Each wheel has a driving and steering motor, and the testbeds rocker-type passive suspension mechanism enables getting over obstacles such as small rocks. The testbed is equipped with an Intel®RealSense™D435 RGB-D sensor, an IMU, wheel encoders for each wheel, and potentiometers between the suspension and the main body. The RGB-D sensor simultaneously captures image and depth information with the resolution and field of view (FOV) shown in Table II. Depth information is calculated by stereo imagery and complemented by projecting infrared patterns. The system configuration is implemented using the Robot Operating System (ROS) and manually steered by using a joystick controller. The controller commands steering motors for turning and driving motors for traveling with angular velocity of at most 0.5 rad/s. When no wheel slip occurs, the testbed can traverse terrain with translational velocity of at most 0.05 m/s.

4.2. Data Collection
Data were collected for five terrain types: *Sand*, *Soil*, *Gravel*, *Asphalt*, and *Cracked-ground*. Fig. 8 shows examples of these terrain types. Dry, cracked terrain is also classified as *Cracked-ground* because the terrain is solid, unlike *Soil* terrain, and is assumed to be

Table I . Specifications of El-Dorado IIB rover testbed.

Size [mm]	L800 $\times$ W650 $\times$ H400
Mass [kg]	23.8
Wheel size [mm]	ϕ 200 $\times$ W100
Wheel base [mm]	600

Fig. 7. El-Dorado IIB rover testbed on sandy terrain. RGB-D sensor, IMU inside the main body, and potentiometers attached to each side of the body are used for acquiring data.

a bedrock region on the surface of Mars. Data for sandy terrain was collected indoors, and data for other terrains were collected outdoors.

Fig. 9 (a), (b) shows the indoor test field. A sandbox is uniformly and loosely covered with dry Toyoura Standard Sand; it can be jacked up manually at an inclination. The testbed motion was tracked using a motion capture camera with accuracy of 1 mm and recording frequency of 100 fps.

Fig. 9 (c), (d) shows the outdoor test fields. For *Soil* and *Gravel* terrains, slopes were made manually. The testbed motion was tracked using a total station with accuracy of 1 mm and recording frequency of 5 fps.

To collect slip versus slope data, the testbed tried to climb the slope for *Sand*, *Soil*, and *Gravel* terrain types. During data collection, image and 3D point cloud data were collected using the RGB-D sensor with recording frequency of 5 fps, posture information was collected by combining data from the IMU and potentiometers, and angular velocity of each wheel was collected from the encoder. The ground truth value of the slope angle was obtained from a digital inclinometer. The slip ratio s was calculated as follows:

$$s = 1 - \frac{v}{r\omega} = 1 - \left(\frac{dx}{dt} \cos\theta + \frac{dz}{dt} \sin\theta \right) \frac{1}{r\omega}, \tag{11}$$

where v is the translational velocity of the testbed; r, the wheel radius; ω, the angular velocity of the wheel; and θ, the slope angle. Proportional–Integral (PI) control was performed for each wheel to rotate at 0.5 rad/s for traveling at 0.05 m/s.

Table II . Specifications of Intel®RealSense^{TM}Depth Camera D435 RGB-D sensor.

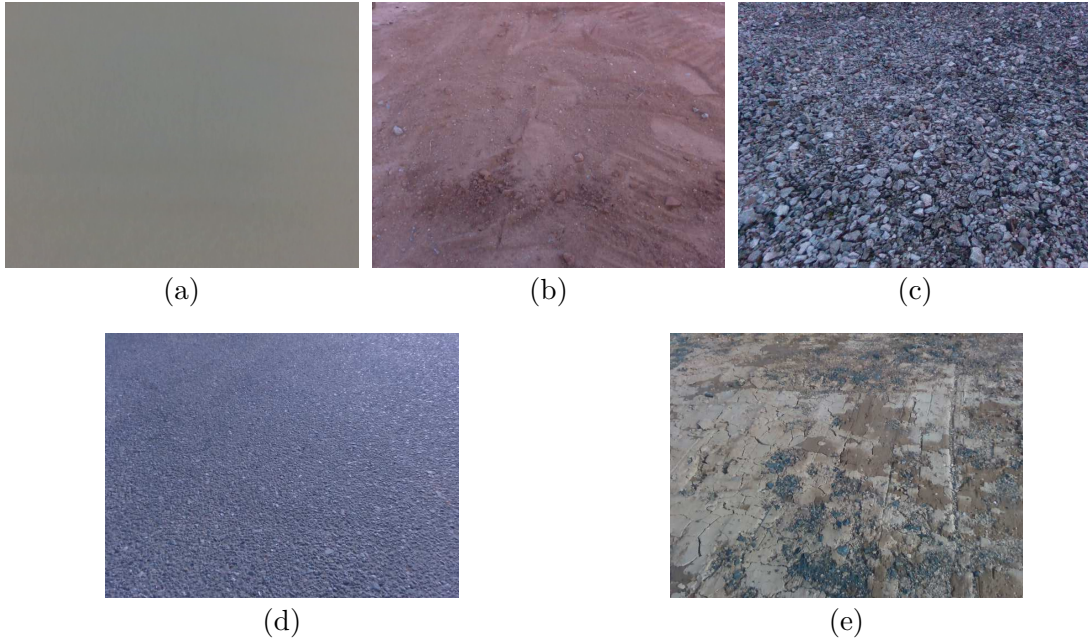|	
Image resolution [pixel]	$320 \times 180 - 1920 \times 1080$
Depth resolution [pixel]	$424 \times 240 - 1280 \times 720$
Frame rate [fps]	$15 - 90$
Measurement range [m]	$0.2 - 10$
Field of view of image sensor [°]	H69.4 $\times$ V42.5 $\times$ D77
Field of view of depth sensor [°]	H85.2 $\times$ V58 $\times$ D94

Fig. 8. Images of different terrain types ((a) *Sand* in indoor test field and (b) *Soil*, (c) *Gravel*, (d) *Asphalt*, and (e) *Cracked-ground* in outdoor test fields) on which the testbed traversed during data collection. Dry, cracked soil was classified as (e) *Cracked-ground* assuming a bedrock region on the surface of Mars.
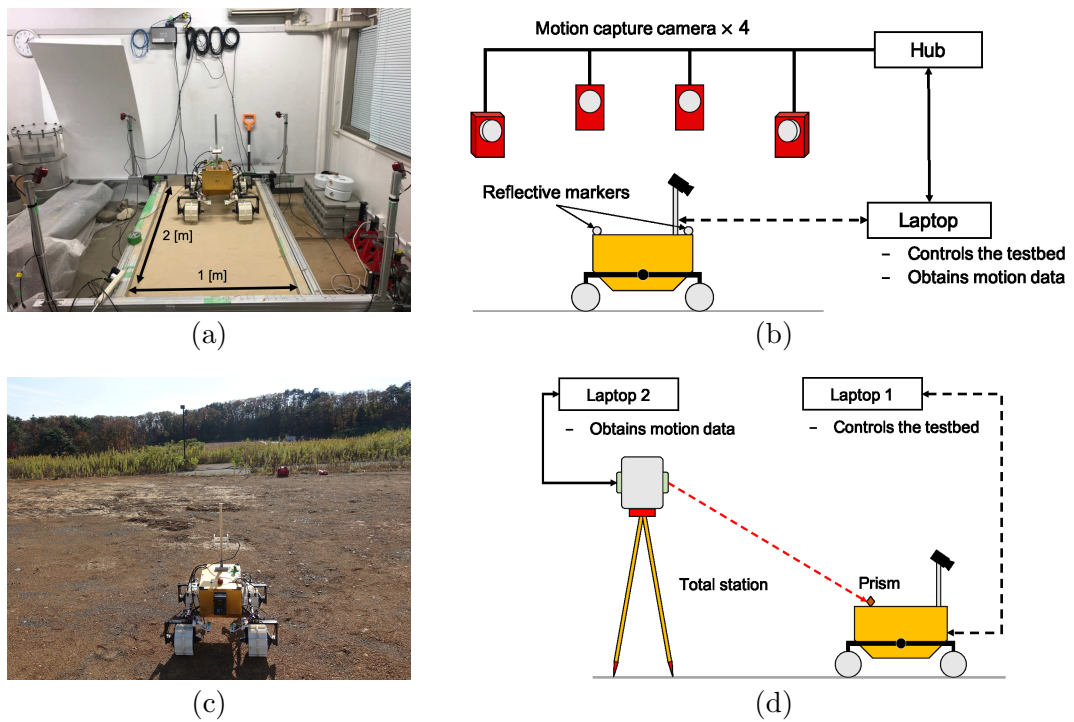

Fig. 9. (a) Indoor test field filled with loose, dry sand. (b) Schematic of indoor experimental setup. (c) Outdoor test fields with smooth soil and cracked-ground surfaces. (d) Schematic of outdoor experimental setup.

4.3. Experimental Conditions

The experimental conditions for terrain classification and slip risk prediction are described below. The MAE of slope estimation for terrain-dependent slip risk prediction is discussed in Section 4.3.2.

4.3.1. Terrain Classification. The classifier was trained on approximately 500 images to predict the terrain type in 25 test images for verification. Five terrain types—*Sand*, *Soil*, *Gravel*, *Asphalt*, and *Cracked-ground*—are contained in respective superpixels. Manually labeled images were also prepared for images including multiple terrain types. When more than half the pixels in a superpixel belonged to one class, the whole superpixel was classified as that class. During classifier training, stratified K-fold cross-validation with $K = 6$ was applied for evaluating the generalization.

4.3.2. Slip Risk Prediction. The regression curve for each terrain was predicted using the collected slip versus slope data. Before optimizing the function, the hyperparameters of the Gaussian basis function $\phi_j(x)$ were set. The maximum slope angle point of each terrain was regarded as the maximum value of μ_j. Other hyperparameters s and j were decided by grid search. To predict slip risk, absolute errors between the ground truth and the estimated value near $s = 0.3$ and $s = 0.6$ were used as the MAE.

5. Results

5.1. Terrain Classification Results

Fig. 10 shows examples of classification results. Fig. 11 shows quantitative results of the terrain classifier as a confusion matrix and a learning curve. By normalizing true positives (TPs), false positives (FPs), true negatives (TNs), and false negatives (FNs), the accuracy (ACC) of each class displayed in the confusion matrix was calculated as follows:

$$ACC = \frac{TP + TN}{TP + TN + FP + FN}. \tag{12}$$

These results indicate that the classifier predicts reasonable classes for each terrain; however, its ability decreases for *Cracked-ground*, as shown in Fig. 11 (a). For instance, for the *Cracked-ground* image in Fig. 10, multiple terrain types including *Cracked-ground* and *Soil* with unclear boundaries are present in the image. Therefore, determining classes is difficult even for a human, and the classifier uses these incorrect results to learn to predict terrain types from the image. This incorrect human labeling is the main cause of reduced accuracy. Fig. 11 (b) shows the generalization performance of the classifier. Two "learning curves" indicates whether the classifier overfits the training data. The green curve representing the cross-validation score approaches the red curve representing the training score. This trend indicates that iterative training using cross-validation improves the classifiers generalization performance.

Table III . Terrain-independent slip versus slope standards for risk prediction.

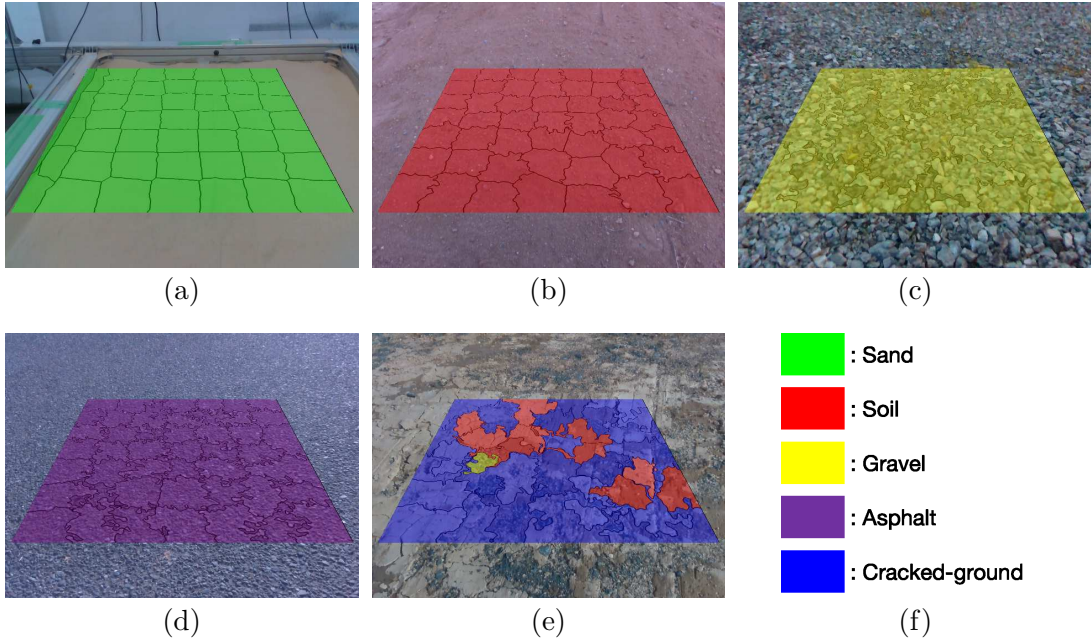| Terrain	MAE	Slip risk	Slip ratio	Slope angle
Sand	0.75	*low*	$s < 0.26$	$\theta < 4.2$
		medium	$0.26 \leq s < 0.55$	$4.2 \leq \theta < 9.3$
		high	$0.55 \leq s$	$9.3 \leq \theta$
Soil	1.15	*low*	$s < 0.23$	$\theta < 12.5$
		medium	$0.23 \leq s < 0.47$	$12.5 \leq \theta < 15.6$
		high	$0.47 \leq s$	$15.6 \leq \theta$
Gravel	1.15	*low*	$s < 0.25$	$\theta < 16.0$
		medium	$0.25 \leq s < 0.53$	$16.0 \leq \theta < 21.5$
		high	$0.53 \leq s$	$21.5 \leq \theta$

Fig. 10. (a), (b), (c), (d), and (e) Examples of classes predicted by terrain classifier for each terrain image. Boundaries in each image indicate the superpixels made by SLIC. (f) Correspondence of classes to color.
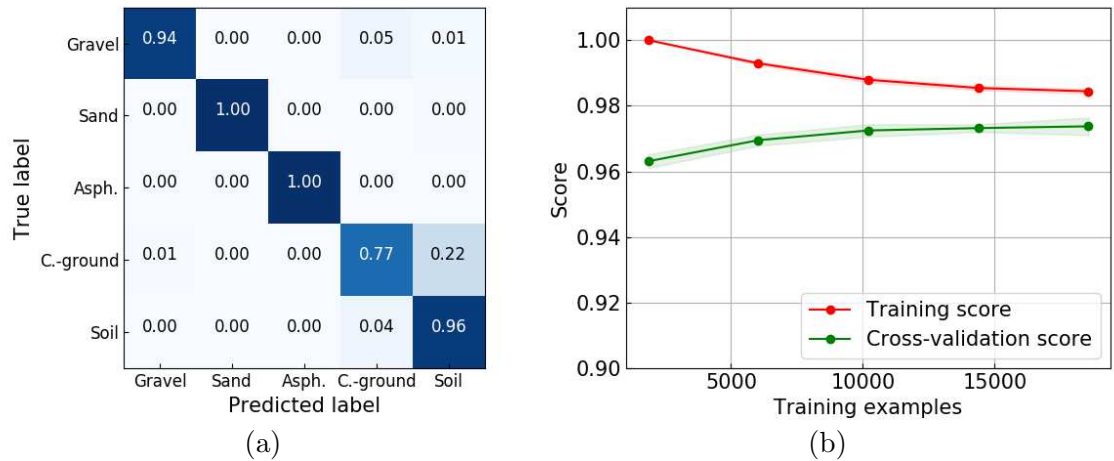

Fig. 11. Summary of ability and validity of terrain classifier. (a) Confusion matrix of terrain classifier with normalization. (b) Learning curve of terrain classifier. Green and red lines indicate the cross-validation score and training score, respectively. Color bands around each line indicate standard deviation of their scores.

5.2. Slip Risk Prediction Results

The slip versus slope relation was acquired using the regression curve and terrain-dependent risk prediction for three terrain types: *Sand*, *Soil*, and *Gravel*. The slip versus slope data obtained during data collection, shown in Fig. 12, indicates that wheel slip trends, such as the rate of slip ratio, depend on terrain properties whereas the slip ratio monotonously increases with increasing slope angle for all terrain types. In *Sand* terrain that comprises homogeneous particles, the slip versus slope relation becomes more linear compared to that in other terrain types. While the wheel gains driving force via grousers pushing away particles in front of the wheel, a larger slope angle increases the slip ratio by drawbar pull.[4] In *Soil* terrain, the slip ratio increases sharply when the
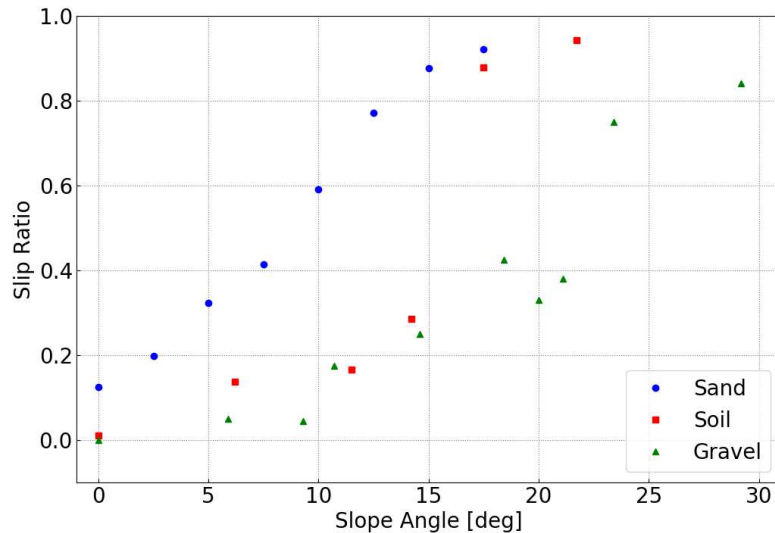
Fig. 12. Input slip versus slope data. Blue, red, and green points indicate data acquired on *Sand*, *Soil*, and *Gravel* terrain, respectively.

slope angle exceeds 15° because the fine grain surface suddenly collapses when the slope angle approaches the internal friction angle of the composition. Further, wheel slip in *Soil* terrain is unlikely to occur because the surface is solid until it breaks up. The *Gravel* terrain also makes the rover travel with low wheel slip compared to that in the case of *Sand* terrain; however, the slip versus slope data is irregular owing to the presence of large, nonuniform particles compared to other terrain types.[15]

Fig. 13 shows a summary of the results for three terrain types. The regression curves for each terrain type fit the monotonic increase of the slip versus slope relation without overfitting the collected data. The thresholds for risk prediction shift from common to terrain-dependent ones using these regression curves, as shown in Table III. Table III also presents the slope estimation accuracy, described in Section 3.1., as an MAE value. The MAE value for each terrain type shows that slope estimation using the RGB-D sensor can well estimate the slope angle in front of the rover. However, such estimation results can still cause problems for the rover; thus, MAE is subtracted from the slope angle corresponding with common thresholds for risk prediction. For *Sand* terrain, the regression curve linearly increases compared to those for *Soil* and *Gravel* terrains; therefore, the thresholds are not significantly affected by the MAE. When the slope angle reaches 9.3°, the slip risk is considered high, and the rover seems to face difficulties in traversing *Sand* terrain. By contrast, the slope of the regression curve for *Soil* terrain suddenly increases at around 17°; therefore, the slip ratio threshold between medium and high risk decreases to 0.13. This sharp increase causes a sudden transition of the slip risk from low to high. In *Gravel* terrain, the regression curve avoids overfitting the irregularity of the slip versus slope relation. Low slip risk, shown as a green region in Fig. 13 (c), indicates that the rover can climb a slope of around 16° safely, whereas it is unable to do so for other terrain types.

6. Conclusion

This study proposes a data-driven approach to predict the slip risk of a rover operating on rough terrain by estimating the slope angle and classifying surrounding terrain using visual information. Terrain-dependent slip risk is predicted by setting the slip-risk criterion for each terrain type in consideration of the slope estimation accuracy. Experimental validation is performed using datasets acquired from a four-wheeled rover testbed traversing different types of rough terrains. The proposed approach can (1)
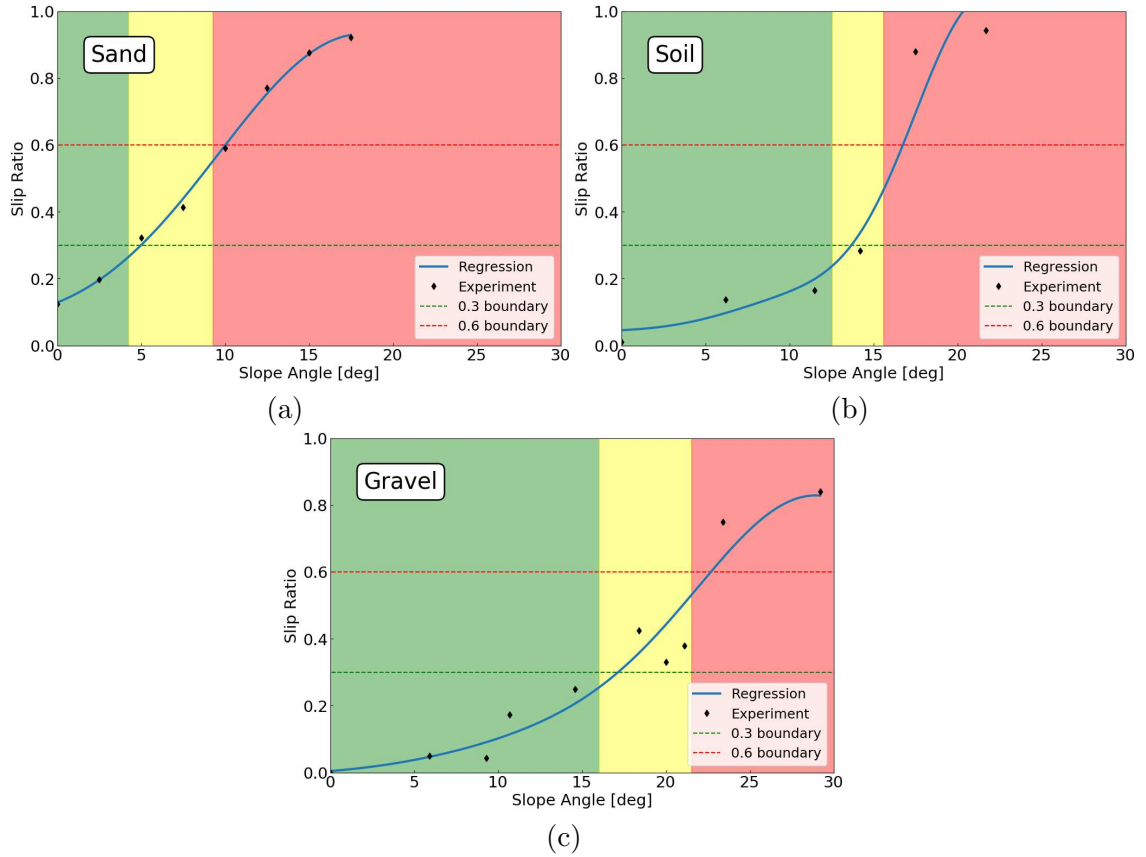
Fig. 13. (a), (b), and (c) Slip risk prediction result for three terrain types: *Sand*, *Soil*, and *Gravel*. Black points indicate input data obtained from data collection. The blue line indicates the predicted regression curve. Green, yellow, and red regions indicate low, medium, and high slip risks, respectively. Green and red dotted lines indicate the common boundaries of low and medium slip and medium and high slip, respectively.

estimate the slope angle within an MAE of $1.15°$, (2) classify five terrain types with at least 77% accuracy, and (3) predict the wheel slip risk on three terrain types in consideration of the slope estimation accuracy, which may be affected by noises such as those contained in 3D information. This study assesses wheel slip and shows that geometrical information alone cannot be used to avoid a wheel getting stuck in the future. It does so by incorporating vision in a mobile robot and introducing terrain-dependent thresholds for the slip versus slope relation.

This study currently uses offline data for both learning and validation. Future studies aimed at autonomous operation will implement online data processing for slip prediction. For this purpose, an adaptive learning procedure will be required to update the slip versus slope relation without overfitting data collected by the rover in early exploration stages or when terrain properties change in a given place even if the appearance of the terrain type does not change.

References

1. S. B. Goldberg, M. W. Maimone, and L. Matthies, "Stereo vision and rover navigation software for planetary exploration," **In**: *Proceedings of the IEEE Aerospace Conference*, Big Sky, MT, USA (2002) pp. 2025–2036.
2. R. E. Arvidson, K. D. Iagnemma, M. Maimone, A. A. Fraeman, F. Zhou, M. C. Heverly, et al., "Mars Science Laboratory Curiosity rover megaripple crossings up to sol 710 in gale crater," *Journal of Field Robotics*, **34**(3), 495–518 (2017).
3. M. G. Bekker, *Introduction to terrain-vehicle systems* (Ann Arbor: University of Michigan Press, USA, 1969).
4. G. Ishigami, K. Nagatani, and K. Yoshida, "Slope traversal controls for planetary rover on sandy terrain," *Journal of Field Robotics*, **26**(3), 264–286 (2009).
5. J. Y. Wong, *Theory of ground vehicles* (John Wiley & Sons, USA, 1978).
6. I. Halatci, C. A. Brooks, and K. Iagnemma "A study of visual and tactile terrain classification and classifier fusion for planetary exploration rovers," *Robotica*, **26**, 767–779 (2008).
7. C. A. Brooks and K. Iagnemma, "Self-supervised terrain classification for planetary surface exploration rovers," *Journal of Field Robotics*, **29**(3), 445–468 (2012).
8. K. Otsu, M. Ono, T. J. Fuchs, I. Baldwin, and T. Kubota "Autonomous terrain classification with co- and self-training approach," *IEEE Robotics and Automation Letters*, **1**(2), 814–819 (2016).
9. L.-P. Berczi, I. Posner, and T. D. Barfoot, "Learning to assess terrain from human demonstration using an introspective gaussian-process classifier," **In**: *Proceedings of the IEEE International Conference on Robotics and Automation*, Seattle, WA, USA (2015) pp. 3178–3185.
10. F. Schilling, X. Chen, J. Folkesson, and P. Jensfelt, "Geometric and visual terrain classfication for autonomous mobile navigation," **In**: *Proceedings of the IEEE/RSJ International Conference on Intelligent Robots and Systems*, Vancouver, BC, Canada (2017) pp. 2678–2684.
11. S. Higa, Y. Iwashita, K. Otsu, M. Ono, O. Lamarre, A. Didier, and M. Hoffman, "Vision-based estimation of driving energy for planetary rovers using deep learning and terramechanics," *IEEE Robotics and Automation Letters*, **4**(4), 3876–3883 (2019).
12. A. Angelova, L. Matthies, D. Heilmick, and P. Perona "Learning and prediction of slip from visual information," *Journal of Field Robotics*, **24**(3), 205–231 (2007).
13. C. Cunningham, M. Ono, I. Nesnas, J. Yen, and W. L. Whittaker, "Locally-adaptive slip prediction for planetary rovers using Gaussian processes," **In**: *Proceedings of the IEEE International Conference on Robotics and Automation*, Singapore, Singapore (2017) pp. 5487–5494.
14. K. Skonieczny, D. K. Shukla, M. Faragalli, M. Cole, and K. D. Iagnemma, "Data-driven mobility risk prediction for planetary rovers," *Journal of Field Robotics*, **36**(2), 475–491 (2019).
15. G. Yamauchi, T. Noyori, K. Nagatani, and K. Yoshida, "Improvement of slope traversability for a multi-DOF tracked vehicle with active reconfiguration of its joint forms," **In** *Proceedings of the IEEE International Symposium on Safety, Security, and Rescue Robotics*, Hokkaido, Japan (2014) pp. 1–6.
16. M. Y. Yang, W. Forstner, "Plane detection in point cloud data," **In** *Proceedings of the 2nd International Conference on Machine Control Guidance*, Bonn, Germany (2010) pp. 95–104.
17. S. Tanaka, K. Yamada, T. Ito, and T. Ohkawa, "Vehicle detection based on perspective transformation using rear-view camera," *International Journal of Vehicular Technology*, **2011** (2011).
18. D. Kim, S. M. Oh, and J. M. Rehg, "Traversability classification for UGV navigation: a comparison of patch and superpixel representations," **In** *Proceedings of the IEEE/RSJ International Conference on Intelligent Robots and Systems*, San Diego, CA, USA (2007) pp. 3166–3173.
19. R. Achanta, A. Shaji, K. Smith, A. Lucchi, P. Fua, and S. Susstrunk, "SLIC superpixel compared to state-of-the-art superpixel methods," *IEEE Transactions on Pattern Analysis and Machine Intelligence*, **34**(11), 2274–2281 (2012).
20. J. H. Friedman "Stochastic gradient boosting," *Computational Statistics & Data Analysis*, **38**(4), pp. 367–378 (2002).
21. W. Y. Loh, "Classification and regression trees," *Wiley Interdisciplinary Reviews: Data Mining and Knowledge Discovery*, **1**(1), 14–23 (2011).
22. R. Gonzalez, M. Fiacchini, and K. Iagnemma, "Slippage prediction for off-road mobile robots via machine learning regression and proprioceptive sensing," *Robotics and Autonomous Systems*, **105**, 85–93 (2018).
23. R. Gonzalez, D. Apostolopoulos, and K. Iagnemma, "Slippage and immobilization detection for planetary exploration rovers via machine learning and proprioceptive sensing," *Journal of Field Robotics*, **35**, 231–247 (2018).
24. D. R. Freitag, A. J. Green, and K. J. Melzer, "Performance evaluation of wheels for lunar vehicles," US Army Waterways Experiment Station Technical Report M-70-2 (Vicksburg, MS, 1970).
25. C. M. Bishop, *Pattern recognition and machine learning* (Springer, USA, 2006).